CrossMark

Terahertz Bistatic Synthetic Aperture Radar for 1-D Near-Field High-Resolution Imaging

Li Ding[1,2,3] (ID) · Yangyang Ye[1] · Guoyao Ye[1] · Yiming Zhu[1,2,3]

Abstract

Considering the difficult transceiver-isolation problem of the monostatic synthetic aperture radar (SAR) in the terahertz (THz) band, this paper proposes a compact THz bistatic SAR (BiSAR) geometry. The system allows the separately distributed transmitter and receivers. At the receiving end, there are a direct-wave receiver and an echo receiver, both operating at the heterodyne and in-phase mode. The echo receiver runs along a linear rail to fulfill the scene scanning, while the direct-wave one is fixed as a reference. Furthermore, assuming that the receivers are synchronized, both the problem of synchronization between the separated transmitter and receivers and the problem of timing at the signal acquisition would be solved by utilizing the high coherence between the echo and the direct wave. Based on such a system, the application of THz BiSAR for one-dimensional imaging is taken into consideration. Then, a high-resolution imaging algorithm is proposed benefitting from the total least squares estimating signal parameters via rotational invariance techniques (TLS-ESPRIT) and the spatial smoothing process (SSP). The imaging performance is then demonstrated by both simulations and the experiments in the 0.183 THz.

Keywords THz imaging · Bistatic SAR · DOA estimation · Synchronization

1 Introduction

Terahertz (THz), which occupies a frequency interval from 0.1 to 10 THz, has a great potential for high-resolution imaging systems [1–3]. The current well-known THz

Li Ding and Yangyang Ye contributed equally to this work.

✉ Yiming Zhu
  ymzhu@usst.edu.cn

1   Shanghai Key Lab of Modern Optical System, University of Shanghai for Science
    and Technology, No. 516 JunGong Road, Shanghai 200093, China

2   Terahertz Technology Innovation Research Institute, Shanghai, China

3   Terahertz Science Cooperative Innovation Center, Shanghai, China

imagers are those utilizing the synthetic aperture radar (SAR) technique [4–6]. For the consideration of the technical maturity and the simplified system establishment in practice, most of the state-of-the-art SAR-based THz imagers prefer to work in a monostatic mode [7, 8]. No matter how many transceivers those systems are utilizing, their inherent property is monostatic, where the transceiver isolation is one of the key factors constraining the imaging performance. Therefore, to ensure the isolation between the transmitters and receivers, bistatic and even multistatic techniques have gained increasing attentions for both long- and short-range THz imaging field nowadays [9].

Compared to monostatic SAR, bistatic SAR (BiSAR) can bring the increased benefits of flexible configuration, abundant information, and reduced vulnerability [10], and has been widely used in the imaging works [11–13]. However, the separated distribution of the transmitter and receiver renders the synchronization to be a significant factor of the imaging performance for BiSAR [14]. In the microwave field, a popular way to implement frequency synchronization is to make all the involved frequencies from a common reference, such as using Global Positioning System disciplined sources [15]. Then, the possible phase synchronization problem would usually be tackled in the post-processing by a mathematical way, such as by compressing the echo signal in the range dimension using the direct signal as a matched filter and by the range cell migration (RCM) [16]. However, there is relatively less consideration of synchronization problem paid on THz BiSAR.

Hence, for THz near-field imaging application, we propose a compact THz BiSAR geometry, where a fixed transmitter emits continuous THz waveform (single-frequency signal or wide-band signal), and a receiving system is of a combination of an echo receiver with a linear motion trajectory and a fixed direct-wave receiver. The receivers operate at a heterodyne- and in-phase mode to reduce the system cost. Although transmitter and receiver are still non-cooperative with each other in our geometry, it is possible to make it synchronized by making use of the strong coherence between the direct wave and the echo. Therefore, the problem of accurate timing existing in the in-phase receiving scheme and the synchronization problem due to the independent transmitter and receivers can be overcome.

Furthermore, based on our proposed system geometry, a one-dimensional (1-D) near-field THz BiSAR imaging is concerned. To obtain an analytical expression for imaging, the Hilbert transform is firstly adopted to convert both the real echo and the direct wave to their complex forms. The strong correlation of the inherent phase relationship between the direct wave and the echo is then utilized to achieve the synchronization. The stationary position method makes the nonlinear phase of the involved route delay a pleasant linear approximation and thus yields the expression for 1-D azimuthal imaging in the wave-number domain.

For the imaging method, the state-of-the-art Fourier transform (FT) algorithms [17], its corresponding resolution would be limited due to the Rayleigh criterion. To break this limitation, a high-resolution imaging method for THz 1-D azimuthal targets is proposed, by combining the direction of arrival (DOA) estimation with the spatial smoothing process (SSP) [18, 19]. Specifically, the total least squares estimating signal parameters via rotational invariance techniques (TLS-ESPRIT) commonly used in the DOA estimation is utilized to improve the azimuth resolution, where

the SSP operates in advance as a pre-processing for TLS-ESPRIT to decrease the coherence of the original data. By establishing the proposed algorithm for high-resolution bistatic radar imaging, we investigate its reconstruction performance by both simulations and experiments.

2 THz BiSAR

2.1 THz BiSAR Geometry

The concerned geometry of THz BiSAR imaging system is shown in Fig. 1. The echo receiver moves on the observation plane and receives the echo signal scattered by the scattering point. The reference receiver which uses the same local oscillator source of the echo receiver is located in a fixed position and receives the direct signal.

The distance from the observation plane to the object plane is R_0. The position of the transmitter is fixed at (x_{tx}, y_{tx}). The echo receiver is placed on a linear rail, and its position is denoted as (x_{rx}, y_{rx}), and x_{rx} ranges from $-\frac{L_x}{2}$ to $\frac{L_x}{2}$, where L_x denotes the aperture length in $x-$dimension and the varying of x_{rx} implies the trajectory of a rectilinear motion. The direct-wave receiver is at a fixed position (x_{ref}, y_{ref}). Both the receivers operate at the heterodyne- and in-phase mode. Obviously, the transmitter and receivers are separately distributed, and the transceiver isolation problem usually troubling the monostatic system does not exist.

2.2 Signal Model for 1-D Imaging

The transmitter sends a single-frequency signal,

$$s_{tx}(t) = \cos(2\pi f_c t + \varphi_{t0}) \tag{1}$$
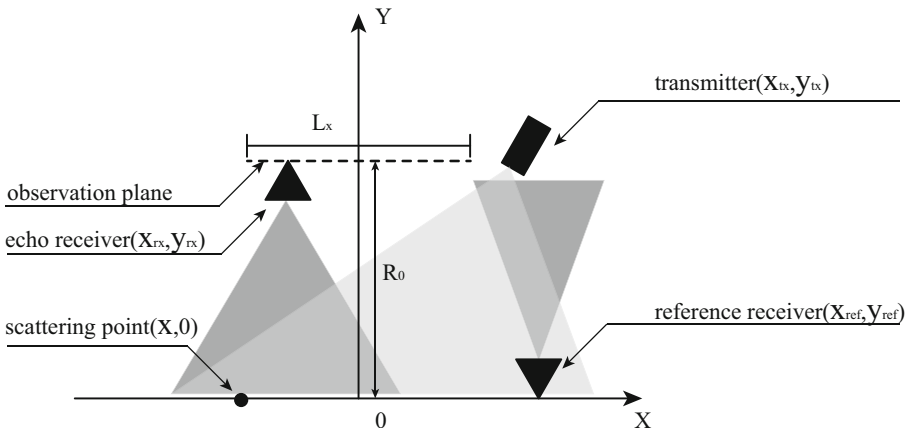
Fig. 1 Geometry of THz BiSAR

where f_c and φ_{t0} denote the carrier frequency and the initial phase at the transmitting end, respectively.

After the propagation delay, the echo is given by

$$s_{rx}(x_{rx}, t) = \int g(x) s_{tx}(t - \tau(x_{rx}, x)) dx \qquad (2)$$

where $g(x)$ denotes the scattering coefficient of a target at $(x, 0)$, $\tau(x_{rx}, x) = \frac{R_t(x) + R_r(x_{rx}, x)}{c}$ is the propagation delay for bistatic, $R_t(x)$ and $R_r(x_{rx}, x)$ represents the distance from the transmitter to the scattering point and that from the scattering point to the echo receiver, respectively, and

$$R_t(x) + R_r(x_{rx}, x) = \sqrt{(x_{tx} - x)^2 + (y_{tx} - 0)^2} + \sqrt{(x_{rx} - x)^2 + (y_{rx} - 0)^2} \quad (3)$$

In receiving, the heterodyne- and in-phase echo receiver has an independently local frequency oscillator, and one of the inputs of its inner mixer can be written as

$$s_{local}(t) = \cos(2\pi f_L t + \varphi_{r0}) \qquad (4)$$

where f_L and φ_{r0} is the local frequency and initial phase at the receiving end, respectively.

Therefore, the output of the mixer with respect to Eqs. 2 and 4 at the echo receiver can be expressed as

$$s_{IF}(x_{rx}, t) = \int g(x) \cos(2\pi f_0 t - 2\pi f_c \tau(x_{rx}, x) + \varphi_{t0} - \varphi_{r0}) dx \qquad (5)$$

where $f_0 = f_c - f_L$ denotes the intermediate frequency.

Similarly, with the same configuration as the echo receiver, the received signal at the direct-wave receiver, denoted as $s_{ref}(t)$, and its corresponding output, denoted as $s_{ref,IF}(t)$, can be expressed respectively as

$$s_{ref}(t) = \cos\left(2\pi f_c \left(t - \frac{R_{ref}}{c}\right) + \varphi_{t0}\right) \qquad (6)$$

$$s_{ref,IF}(t) = \cos\left(2\pi f_0 t - \frac{2\pi f_c R_{ref}}{c} + \varphi_{t0} - \varphi_{r0}\right) \qquad (7)$$

where R_{ref} is the reference distance from transmitter to reference receiver and is of the form as

$$R_{ref} = \sqrt{(x_{ref} - x_{tx})^2 + (y_{ref} - y_{tx})^2} \qquad (8)$$

It is easily observed from Eq. 5 that as a continuous signal, the start timing of signal acquisition for the echo when in-phase mode is adopted and the initial phase mismatch induced by φ_{r0} and φ_{t0} make it hard to achieve inversion of $g(x)$ from Eq. 5. However, it can be solved by jointly utilizing the direct wave.

Hence, we firstly turn the involved real signals to their complex forms, and thus, the Hilbert transform is taken into consideration. Correspondingly, the echo in Eq. 5 and the direct wave in Eq. 7 can be rewritten as

$$s_{Hilbert}(x_{rx}, t) = \text{Hilbert}\{s_{IF}(x_{rx}, t)\} = \int g(x)e^{j(2\pi f_0 t - 2\pi f_c \tau(x_{rx}, x) + \varphi_{t0} - \varphi_{r0})}dx \tag{9}$$

$$s_{ref,Hilbert}(t) = \text{Hilbert}\{s_{ref,IF}(t)\} = e^{j(2\pi f_0 t - \frac{2\pi f_c R_{ref}}{c} + \varphi_{t0} - \varphi_{r0})} \tag{10}$$

where Hilbert$\{\cdot\}$ represents the Hilbert transform.

Then the direct wave can be made as a matched filter, and the possible synchronization problem existed in echo (i.e., Eq. 9) can be alleviated by a conjugate multiplication between (9) and (10),

$$s(x_{rx}) = s_{Hilbert}(x_{rx}, t)s^*_{ref,Hilbert}(t) = \int g(x)e^{jk(R_{ref} - (R_t(x_{rx}) + R_r(x_{rx}, x)))}dx \tag{11}$$

where $(\cdot)^*$ represents the conjugate operation and $k = \frac{2\pi f_c}{c}$ indicates the wavenumber.

To obtain an analytical expression for 1-D imaging, firstly the Fourier transform of Eq. 11 is operated along the observation aperture to turn the echo into the wavenumber domain, i.e.,

$$S(k_x) = \int s(x_{rx})e^{-jk_x x_{rx}}dx_{rx} \tag{12}$$

where k_x represents the component of the wavenumber frequency in the x dimension.

Let the phase in Eq. 12 be $\varphi(x, x_{rx}) = k(R_t(x) + R_r(x_{rx}, x)) + k_x x_{rx} - kR_{ref}$. According to the principle of stationary position method, the integral of $\varphi(x, x_{rx})$ can get its non-zero value around x^*_{rx}, we can get

$$\varphi(x, x^*_{rx}) = k\sqrt{(x_{tx} - x)^2 + y^2_{tx}} + k_x x + \sqrt{k^2 - k^2_x}y_{rx} - kR_{ref} \tag{13}$$

So far, substituting (13) into (12) yields the signal model for 1-D imaging.

$$S^*_{FT}(k_x) = \int g(x)e^{-j\left(k\sqrt{(x_{tx} - x)^2 + y^2_{tx}} + k_x x + \sqrt{k^2 - k^2_x}y_{rx} - kR_{ref}\right)}dx \tag{14}$$

Since y_{rx} and R_{ref} are known parameters in Eq. 13, their corresponding terms $e^{-j\sqrt{k^2 - k^2_x}y_{rx} + jkR_{ref}}$ in Eq. 14 can be removed through a phase-compensation.

$$S_{comp}(k_x) = S^*_{FT}(k_x)e^{j\sqrt{k^2 - k^2_x}y_{rx} - jkR_{ref}} = \int g(x)e^{-j\left(k\sqrt{(x_{tx} - x)^2 + y^2_{tx}} + k_x x\right)}dx \tag{15}$$

3 High-Resolution 1-D Imaging Method

To achieve high-resolution imaging, the TLS-ESPRIT is taken into account. We firstly turn the signal in Eq. 15 to its discrete way, and then the signal received at the m-th spatial sampling position can be written as

$$s_m = \sum_{k=1}^{K} g(x_k) e^{-jk(\sqrt{(x_{tx}-x_k)^2+y_{tx}^2})-jm\Delta k_x x_k} \tag{16}$$

where $m = 1, ..., M$ and M is the number of sampling positions, K is the number of scattering points in the scene of interested, Δk_x represents the sampling interval of the X-dimensional wavenumber domain and $\Delta k_x = \dfrac{kL_x}{M\sqrt{\left(\frac{L_x}{2}\right)^2+R_0^2}}$.

By collecting the signals from all of the sampling positions, and defining

$$\mathbf{s} = [\, s_1 \ s_2 \ \dots \ s_M \,]^T$$

we can get the following simplified expression

$$\mathbf{s} = \mathbf{ADg} \tag{17}$$

where

$$\mathbf{g} = [g(x_1), \cdots, g(x_K)]^T$$
$$\mathbf{D} = diag\left\{ e^{-jk\sqrt{(x_{tx}-x_1)^2+y_{tx}^2}}, \cdots, e^{-jk\sqrt{(x_{tx}-x_K)^2+y_{tx}^2}} \right\}$$
$$\mathbf{A} = [\mathbf{a}_1, \cdots, \mathbf{a}_M]^T$$
$$\mathbf{a}_m = [e^{-jm\Delta k_x x_1}, \cdots, e^{-jm\Delta k_x x_K}]^T$$

where $(\cdot)^T$ represents transpose and $\mathbf{a}_m$ denotes the receiving steering vector.

– Step 1: Spatial smoothing process (SSP)

   In order to effectively reduce the interference of the high coherent signal involved in Eq. 16, SSP method is adopted. As illustrate in Fig. 2, the signal
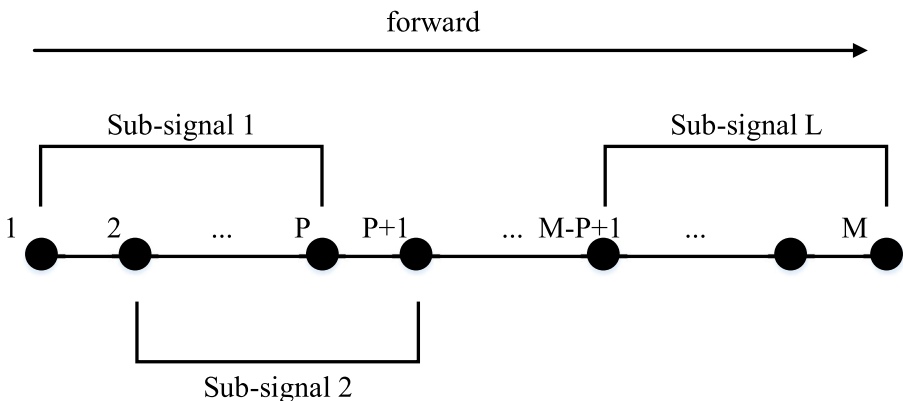
Fig. 2 Spatial smoothing process

is segmented into L ($L = M + 1 - P$) vectors, where P is the length of the sub-signal, $P \in \{2, 3, ..., M - 1\}$. Let the l-th sub-signal be denoted as

$$\mathbf{s}_l = \begin{bmatrix} s_l & \cdots & s_{l+p} & \cdots & s_{l+P-1} \end{bmatrix}^T \tag{18}$$

where s_{l+p} represents the $(p + 1)$-th element belonging to the l-th sub-signal, and $s_{l+p} = \mathbf{a}_{l+p}^T \mathbf{g}$, $1 \leqslant l \leqslant L$, $0 \leqslant p \leqslant P - 1$.

– Step 2: Covariance matrix construction

Then, the average of all sub-signal covariance matrixes would be obtained as

$$\mathbf{R}_{ss} = \frac{1}{L} \sum_{l=1}^{L} \mathbf{s}_l (\mathbf{s}_l)^H \tag{19}$$

where $(\cdot)^H$ represents conjugate transpose.

– Step 3: Eigenvalue Decomposition

$\mathbf{R}_{ss}$ can be decomposed as

$$\mathbf{R}_{ss} = \mathbf{E}_{ss} \boldsymbol{\Lambda} \mathbf{E}_{ss}^H \tag{20}$$

where $\boldsymbol{\Lambda}$ is the diagonal matrix consisting of eigenvalues, $\mathbf{E}_{ss}$ is the corresponding matrix consisting of eigenvectors. Then, we form $\mathbf{E}_x$ and $\mathbf{E}_y$ from $\mathbf{E}_{ss}$ as

$$\begin{aligned} \mathbf{E}_x &= \mathbf{E}_{ss}(:, 1 : M - 1) \\ \mathbf{E}_y &= \mathbf{E}_{ss}(:, 2 : M) \end{aligned} \tag{21}$$

Equation (21) is to build two new eigenvectors $\mathbf{E}_x$ and $\mathbf{E}_y$ from the original eigenvector $\mathbf{E}_{ss}$. And the new eigenvector has a fixed phase difference between each element.

– Step 4: Noise subspace construction

Letting $\mathbf{E}_s = \begin{bmatrix} \mathbf{E}_x \\ \mathbf{E}_y \end{bmatrix}$, we can get the decomposition of $\mathbf{E}_s \mathbf{E}_s^H \in \mathbb{C}^{2P \times 2P}$

$$\mathbf{E}_s \mathbf{E}_s^H = \mathbf{E} \boldsymbol{\Lambda}_s \mathbf{E}^H \tag{22}$$

where $\boldsymbol{\Lambda}_s$ is the diagonal matrix composed of eigenvalues, and $\mathbf{E}$ is a matrix of its corresponding eigenvectors.

Furthermore, dividing the matrix $\mathbf{E}$ into four $P \times P$ sub-matrices, that is

$$\mathbf{E} = \begin{bmatrix} \mathbf{E}_{11} & \mathbf{E}_{12} \\ \mathbf{E}_{21} & \mathbf{E}_{22} \end{bmatrix} \tag{23}$$

where $\begin{bmatrix} \mathbf{E}_{11} \\ \mathbf{E}_{21} \end{bmatrix} \in \mathbb{C}^{2P \times P}$ consists of the eigenvectors corresponding to larger sigenvalues, and $\begin{bmatrix} \mathbf{E}_{12} \\ \mathbf{E}_{22} \end{bmatrix} \in \mathbb{C}^{2P \times P}$ consists of the eigenvectors corresponding to the left smaller eigenvalues, denoting the noise subspace.

– Step 5: DOA estimation

Letting $\boldsymbol{\Psi} = -\mathbf{E}_{12} \mathbf{E}_{22}^{-1}$, the eigenvalues of $\boldsymbol{\Psi}$ can be computed as $\left\{ \hat{\phi}_1, \cdots, \hat{\phi}_P \right\}$. Assuming that the eigenvalues are sorted in a descending order,

the position of the scatterer can be calculated from its K largest eigenvalues as follows

$$\hat{x}_k = \left\{ \frac{angle(\hat{\phi}_k)}{\Delta k_x} \right\}, \quad k = 1, 2, ..., K \tag{24}$$

where $angle(\cdot)$ represents the extraction phase.

The scattering coefficient $g(x_k)$ can be obtained by bringing the estimated x_k into the measurement matrix $\mathbf{A}$ in Eq. 17, i.e.,

$$\hat{\mathbf{g}} = \mathbf{D}^{-1}(\mathbf{A}^H\mathbf{A})^{-1}\mathbf{A}^H s \tag{25}$$

4 Simulations

We compare the performance of the proposed algorithm with FT-based algorithm, especially from the actual azimuth resolution point of view.

The spatial sampling interval based on Nyquist theory is approximated as

$$\Delta x^* \approx \frac{\lambda}{2} \tag{26}$$

where λ denotes the wavelength, and $\lambda = \frac{c}{f_c}$.

The theoretical azimuth resolution is given by

$$\delta \approx \frac{c\sqrt{R_0^2 + \left(\frac{L_x}{2}\right)^2}}{f_c L_x} \tag{27}$$

The parameters are listed in Table 1.

a) Imaging based on simulations

When the synthetic aperture length of BiSAR L_x is fixed, the simulations have been carried out to illustrate the influence of spatial sampling interval on imaging performance of two algorithms. Here three scatterers are located at $(-2.1\text{cm},0\text{cm})$, $(-1.8\text{cm},0\text{cm})$ and $(4\text{cm},0\text{cm})$, respectively, where the distance between any two scatterers is multiple times of the resolution.

Table 1 Parameters

Parameter	Value
Carrier frequency f_c	183GHz
Local frequency f_L	182GHz
Position of reference receiver (x_{ref}, y_{ref})	(0.2m,0m)
Position of transmitter (x_{tx}, y_{tx})	(0.2m,0.5m)
Distance from observation plane to object plane R_0	0.5m
The aperture length L_x	0.3m
Nyquist sampling interval Δx^*	0.8mm
Theoretical azimuth resolution δ	3mm
Signal-to-noise ratio	10dB

(a) Imaging results

(b) Influence of the distance between two scatters on the relative estimation error
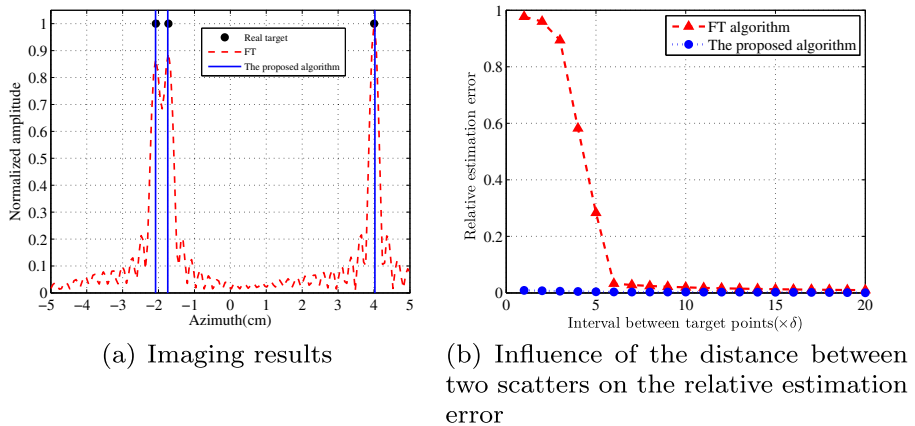
Fig. 3 Performance comparison between our proposed algorithm and FT

It is apparent from Fig. 3a that both the algorithms can accurately reconstruct the scatterers when the distance between two scatterers is greater than the azimuth resolution. When two scatterers become closer with a small interval, like one theoretical resolution, the performance of FT-based algorithm would be deteriorated due to the influence of mainlobe and sidelobe. However, the proposed algorithm maintains its performance.

Then, the estimation error of the two algorithms versus the varying distance between two scatterers is examined. According to Fig. 3b, we can see that the performance of FT-based algorithm gradually becomes well with the increasing interval of the two scatterers, especially when the distance is great than 6δ. However, the estimation error of the proposed algorithm keeps stable at a very small value, even in the case of two scatterers with their interval less than theoretical resolution δ. This
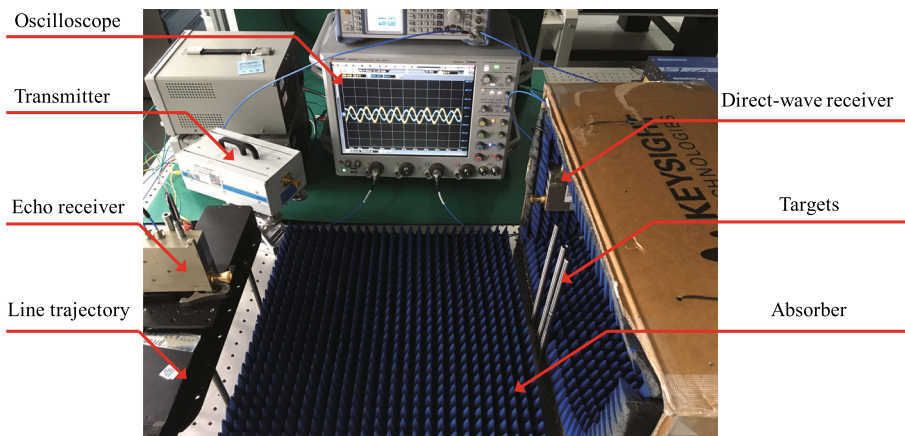
Fig. 4 Photograph of the THz BiSAR experimental system

(a) Photograph of multiple cylinders
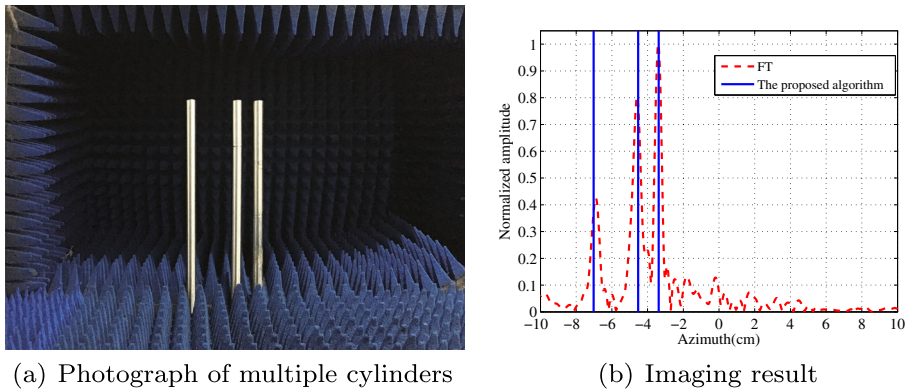
(b) Imaging result

Fig. 5 Imaging result for multiple cylinders

implies that the proposed algorithm can guarantee an improved resolving capability in contrast to FT-based counterpart.

b)   Imaging based on experiments

To perform proof-of-principle experiments, a prototype imager with the same parameters setting in Table 1 is established as Fig. 4 shows. The echo and direct wave are acquired simultaneously by a two-channel oscilloscope.

Firstly, there are three mental cylinders with the same diameter of 1.5cm as the targets under test, shown in Fig. 5a. At this time, the distance between any two scatterers are greater than multiple times of resolution. The 1-D imaging result is shown in Fig. 5b, it is obvious to see that the targets can be clearly identified by both algorithms.

To test the practical resolution, two cylinders are placed with 3mm interval as the targets, shown in Fig. 6a. Obviously, Fig. 6b demonstrates that the targets can be well resolved by the proposed algorithm when the interval between the two metal

(a) Photograph of two cylinders
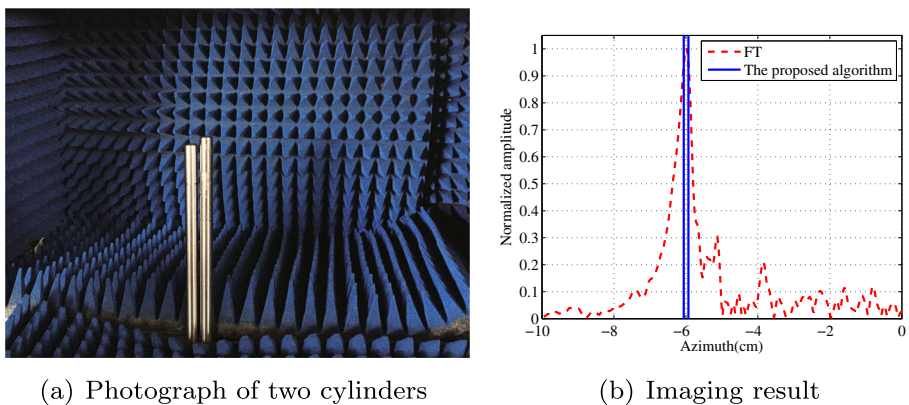
(b) Imaging result

Fig. 6 Imaging result for two cylinders

cylinders is equal to the theoretical resolution, while the FT-based algorithm fails. This exactly verifies the good performance of our proposed algorithm.

5 Conclusion

In this paper, a compact THz bistatic SAR geometry has been proposed for the difficult transceiver-isolation problem in the monostatic SAR with application to THz imaging. Benefitting from the proposed geometry, the problem of synchronization for bistatic system and the problem of accurate timing in in-phase receiving scheme have been solved mathematically by utilizing the high coherence between the echo and the direct wave. Then, a proposed algorithm based on TLS-ESPRIT and SSP has been performed to support high-resolution 1-D imaging from DOA estimation point of view. The simulations and experiment results demonstrate that compare with FT-based algorithm, the proposed algorithm is able to provide better resolution performance, and this shows its wide feasibility in practical applications.

References

1. Liu H. B., Zhong H., Karpowicz N., et al., Terahertz spectroscopy and imaging for defense and security applications. *Proceedings of the IEEE* 95(8): 1514–1527 (2007).
2. Catapano I, Soldovieri F, Mazzola L, et al., THz Imaging as a method to detect Defects of aeronautical coatings. *Journal of Infrared, Millimeter, and Terahertz Waves* : 1–14 (2017).
3. Ouchi T., Kajiki K., Koizumi T., et al., Terahertz imaging system for medical applications and related high efficiency terahertz devices. *Journal of Infrared, Millimeter, and Terahertz Waves* 35(1): 118–130 (2014).
4. Flammini, Mariano, et al., Confocal terahertz imaging of ancient manuscripts. *Journal of Infrared, Millimeter, and Terahertz Waves* 38.4: 435–442 (2017).
5. Ni J., Zhang Q., Yang Q., et al., Directional feature: a novel feature for group target detection in high resolution SAR images. *Remote Sensing Letters* 8(8): 713–722 (2017).
6. Liu G., Guo H., Yue H., et al., Modified four-pass differential SAR interferometry for estimating mountain glacier surface velocity fields. *Remote Sensing Letters* 7(1): 1–10 (2016).
7. Jackson J. A., Moses R. L., Feature extraction algorithm for 3D scene modeling and visualization using monostatic SAR. *Defense and Security Symposium. International Society for Optics and Photonics*: 623708-623708-12 (2006).
8. Wang R., Deng Y. K., Loffeld O., et al., Processing the azimuth-variant bistatic SAR data by using monostatic imaging algorithms based on two-dimensional principle of stationary phase. *IEEE Transactions on Geoscience and Remote Sensing* 49(10): 3504–3520 (2011).
9. Hu K., Zhang X., Shi J., et al., Image reconstruction method for stepped-frequency multichannel bistatic SAR. *Remote Sensing Letters* 8(1): 48–57 (2017).
10. Walterscheid I., Ender J., Brenner A. R., et al., Bistatic SAR processing and experiments. *IEEE Transactions on Geoscience and Remote Sensing* 44(10): 2710–2717 (2006).
11. Cherniakov M., Zeng T., Plakidis E., Ambiguity function for bistatic SAR and its application in SS-BSAR performance analysis. *Radar Conference, 2003. Proceedings of the International. IEEE*: 343—348 (2003).

12. Klare J., Walterscheid I., Brenner A., et al., Evaluation and optimisation of configurations of a hybrid bistatic SAR experiment between TerraSAR-X and PAMIR. *Geoscience and Remote Sensing Symposium, 2006. IGARSS 2006. IEEE International Conference on. IEEE*: 1208—1211 (2006).
13. Moccia A., Rufino G., De Luca M., Oceanographic applications of spaceborne bistatic SAR. *Geoscience and Remote Sensing Symposium, 2003. IGARSS'03. Proceedings. 2003 IEEE International. IEEE*: 1452—1454 (2003).
14. Hong F., Wang R., Zhang Z., et al., Integrated time and phase synchronization strategy for a multichannel spaceborne-stationary bistatic SAR system. *Remote Sensing* 8(8): 628 (2016).
15. Lombardi M. A., Nelson L. M., Novick A. N., et al., Time and frequency measurements using the global positioning system. *Cal Lab: International Journal of Metrology* 8(3): 26—33 (2001).
16. Zhang M., Wang R., Deng Y., et al., A synchronization algorithm for spaceborne/stationary BiSAR imaging based on contrast optimization with direct signal from radar satellite. *IEEE Transactions on Geoscience and Remote Sensing* 54(4): 1977-1989 (2016).
17. Sheen D. M., McMakin D. L., Hall T. E., Three-dimensional millimeter-wave imaging for concealed weapon detection. *IEEE Transactions on microwave theory and techniques* 49(9): 581—1592 (2001).
18. Zhang S., Zhang Y., Wang W. Q., et al., Sparsity-inducing super-resolution passive radar imaging with illuminators of opportunity. *Remote Sensing* 8(11): 929 (2016).
19. Yang T., Wang Y., Chen G., Digital beamforming in elevation for spaceborne HRWS SAR based on sparse DOA estimation. *Remote Sensing Letters* 8(5): 448—457 (2017).